International Journal of Heat and Mass Transfer 224 (2024) 125325

Contents lists available at ScienceDirect

International Journal of Heat and Mass Transfer

journal homepage: www.elsevier.com/locate/ijhmt

Charging and discharging in thermal energy storage unit with fin-stone hybrid structure for enhancing heat transfer of phase change materials

Shuai Zhang [a], Yuying Yan [a,*], Ziming Cheng [b], Fuqiang Wang [b]

[a] Faculty of Engineering, University of Nottingham, University Park, Nottingham, UK
[b] School of New Energy, Harbin Institute of Technology at Weihai, 2, West Wenhua Road, Weihai 264209, PR China

ARTICLE INFO

Keywords:
Fin-stone hybrid structure
Heat transfer enhancement
Phase change material
Shell-and-tube

ABSTRACT

This work proposes a fin-stone hybrid structure integrating fins (popular thermal enhancers) and natural stones (widely used sensible heat storage media) to enhance the heat transfer of phase change materials for on-site thermal energy storage applications, with advantages of low cost, environmental friendliness, and easy accessibility. 3D numerical models of charging and discharging in shell-and-tube heat storage units with various configurations, including fins, the fin-stone hybrid structure, stones, and no heat transfer enhancement, were constructed, and the performance evaluation and comparison were carried out. Compared to fins, fin-stone hybrid structures with 20 mm-, 30 mm-, and 40 mm-sized stones shorten the charging time by 67%, 54%, and 56%, and the discharging time by 73%, 60%, and 46%, respectively. Small stones have better heat transfer enhancement, which is attributed to the small volume, large surface area, and contact with the tube and fins. The advantage of the fin-stone hybrid structure, i.e. the shortening of phase change time, is more significant in charging than in discharging, in comparison with stones, as both heat conduction and natural convection are enhanced. Moreover, the hybrid structure exhibits satisfactory temperature stability with a 48.9 °C temperature change in charging and 37.2 °C in discharging, each lower than the fins, which is beneficial to stabilise the heat transfer fluid outlet temperature. The yearly supplied energy of the hybrid structure with 20 mm-sized stones is 121% and 72% more than that of fins and stones, respectively.

1. Introduction

Using renewable energy is one of the approaches to the global energy crisis and environmental pollution [1–3]. Renewable energy resources such as solar energy are abundant, easily accessible, and green [4,5]; however, they usually have drawbacks of instability and intermittence [6,7]. To solve these problems, thermal energy storage (TES) has been proposed, which can store unstable thermal energy and release stable thermal energy [8–10]. Moreover, thermal energy is stored and then released at the desired time, solving the temporal mismatch between energy supply and demand.

Natural stones, typical sensible heat storage materials (SHMs), are widely accessible, low-cost, and environmentally friendly as they do not need additional material fabrication. Moreover, their thermal conductivity is high, and the energy storage rate is high [11]. Natural stones are mostly used as SHMs in packed beds where the heat transfer fluid (HTF) flows through a stack of stones and transfers heat to or extracts heat from them. Audi [12] conducted experiments to investigate using Jordanian stones for storage in solar space heating. The required volume of different types of stones was determined. Tiskatine et al. [13] evaluated fifty-two types of stones used for concentrated solar power and assessed multiple criteria, including compressive strength, density, thermal cycling resistance, thermal capacity, and thermal conductivity. Sandstone, gabbro, and dolerite were found to be superior high-temperature thermal energy storage media. Lugolole et al. [14] investigated granite with different sizes as SHMs in a packed bed thermal energy storage system and found that big stones had a higher exergy rate than small ones. Soprani et al. [15] studied the charging and discharging of a packed bed heat storage tank filled with 16–22 mm sized diabase. Various charging powers, flow conditions, and bed configurations were evaluated, and the influence of the buoyancy force on the temperature gradient was analysed. Singh et al. [16] built a packed bed heat storage tank filled with pebbles and investigated the thermal performance under different solar conditions. They point out that the solar collection efficiency of the heat storage tank with 8500 kg pebbles was 43.5% on average over March, April, and May.

Phase change material (PCM) is a more attractive thermal energy

* Corresponding author.
E-mail address: Yuying.Yan@nottingham.ac.uk (Y. Yan).

https://doi.org/10.1016/j.ijheatmasstransfer.2024.125325
Received 28 October 2023; Received in revised form 22 January 2024; Accepted 11 February 2024
Available online 14 February 2024

Nomenclature

HTF	heat transfer fluid
PCM	phase change material
SHM	sensible heat storage material
TES	thermal energy storage
A_{mushy}	mushy zone constant, kg/(m^3·s)
c_p	specific heat capacity, J/(kg·K)
D	yearly operating time of a heat storage unit, s
D_{stone}, N_{stone}	diameter and number of stones, mm, -
g	gravitational acceleration, m/s^2
H_{fin}, τ_{fin}	height and thickness of fins, mm, mm
L	latent heat of the PCM, J/kg
L_f	liquid fraction, -
Lunit	length of the heat storage unit, mm
p	pressure, Pa
Q_{HTF}	flow rate of the HTF, L/min
Q_{res}	energy released in discharging, kJ
Q_{year}	yearly supplied energy, kJ
t_{full}	time of full charging and discharging, s
T	temperature, K
T_{ini}	initial temperature,°C
$T_{m,\,s}$, $T_{m,\,l}$	solidus and liquidus temperatures of the PCM, K
u, v, w	velocity components in x, y, and z directions, m/s
U	velocity vector, m/s

Greek letter

μ	viscosity, Pa·s
ε	volume fraction of the PCM, -
β	thermal expansion coefficient, K^{-1}
ω	a small number (0.001)
φ	liquid fraction in a single cell, -
ρ	density, kg/m^3
k	thermal conductivity, W/(m·K)
Ω	outer surface of the heat storage unit

Subscripts

f	fluid
PCM	phase change material
HTF	heat transfer fluid

storage medium owing to its high energy density [17]. However, one of the problems with the PCM is the low thermal conductivity, which leads to a long charging/discharging time and a low energy storage rate [18]. Using porous skeletons, fins, heat pipes, and particles are popular methods to enhance the heat transfer of the PCM. Porous skeletons, such as copper foam [19,20], aluminium foam [21,22] and SiC ceramic foam [23,24], have a large surface area and can be in contact with the PCM fully. Heat pipes, which act as bridges between the HTF and PCM, increase the heat transfer area [25]. Particles, including aluminium powder [26], copper oxide nanoparticles [27], and carbon nanotubes [28], have high thermal conductivity; however, particles are found to harm the heat transfer performance of the PCM in some studies because the suppression of natural convection is greater than the improvement in the effective thermal conductivity [29]. Fins enhance heat transfer by increasing the contact area, and their fabrication is simpler than porous skeletons and heat pipes [30]. Moreover, maintenance is easy since fins are separate from one another; if one fin fails, only that fin, rather than all ones, needs to be maintained. These advantages lower the cost of using fins.

The research of using fins generally focuses on two aspects. The first one is to optimise configurations of conventional fins (longitudinal and radial), including number, height, thickness, position, and angle. Yang et al. [31] investigated the influence of fin numer on the charging in a horizontal heat storage unit, and Joybari et al. [32] studied the simultaneous charging and discharging in a triplex tube heat storage unit. Their studies indicate that increasing the number and height of fins can accelerate thermal energy storage by extending the contact area [31], while the thickness of fins has little effect on thermal energy storage [32]. Natural convection plays an important role in phase change heat; hence, Wang et al. [33] and Tao et al. [34] investigated the effect of natural convection. They found that natural convection at the upper half is stronger than at the lower half in the melting process, so fins are preferred to weld on the lower half of the tube to reduce the suppression of natural convection [33,34]. In terms of the fin angle, Liu and Groulx [35]'s experimental results concerning a horizontal heat storage unit suggest that fins with 45° rotation are superior to the straight ones (horizontal and vertical) for the melting process; by contrast, there is almost no difference for the solidification process.

The second research focus is to design fins with novel shapes, such as tree-shaped [36], snowflake-shaped [37], ladder-shaped [38,39], herringbone-shaped [40], V-shaped [41], Y-shaped [42], etc. Those novel fins have a large contact area, further enhancing heat transfer. Taking the ladder-shaped fin as an example, the volume is the same as conventional fins, but the contact area with the PCM is increased by about two times, leading to a higher melting rate. Moreover, these novel fins can be further optimized according to length, width, angle, etc. The tree-shaped fin designed by Zhang et al. [36] mimicked the leaf venation and shortened the solidification time by 66.2%. Herringbone wavy fins proposed by Sharma et al. [40] were compared to conventional longitudinal fins and were found to save 22% solidification time. Sheikholeslami et al. [41] integrated V-shaped fins and copper oxide nanoparticles in a shell-and-tube heat storage unit. Various factors were evaluated, including nanoparticle size, concentration, fin angle, and length. A spider web-shaped fin with a greatly extended surface area was developed by Wu et al. [43] recently, where the shape is similar to the porous skeleton.

Many researchers have investigated using natural stones as sensible heat storage media and fins as thermal enhancers. However, there are few studies integrating these two materials, i.e. the fin-stone hybrid structure. This novel structure has the following advantages: (1) natural stones have high thermal conductivity and can further enhance the heat transfer of the PCM; (2) stones are naturally accessible and using them is environmentally friendly; (3) natural stones are low-cost, the same as fins, which strengthens the cost advantage. There are very few studies using the fin-stone hybrid structure to enhance the heat transfer of the PCM. The lack of knowledge of the fin-stone hybrid structure leads to a poor understanding of its performance and hampers its potential applications. Thus, it is essential to investigate the fin-stone hybrid structure. In this study, three-dimensional numerical models of the typical shell-and-tube heat storage units with the fin-stone hybrid structure enhancing the heat transfer of the PCM were constructed. Charging and discharging were simulated, where solid-liquid interface propagation, temperature response, and energy storage performance were assessed. The fin-stone hybrid structure proposed in this study has the advantages of low cost, environmentally friendliness, and easy installation. This study fills in the knowledge gap and provides comprehensive heat transfer enhancement information on the novel fin-stone hybrid structure, guiding its applications for on-site thermal energy storage systems.

2. Numerical model

2.1. System configuration

The shell-and-tube heat storage unit with the PCM occupying the

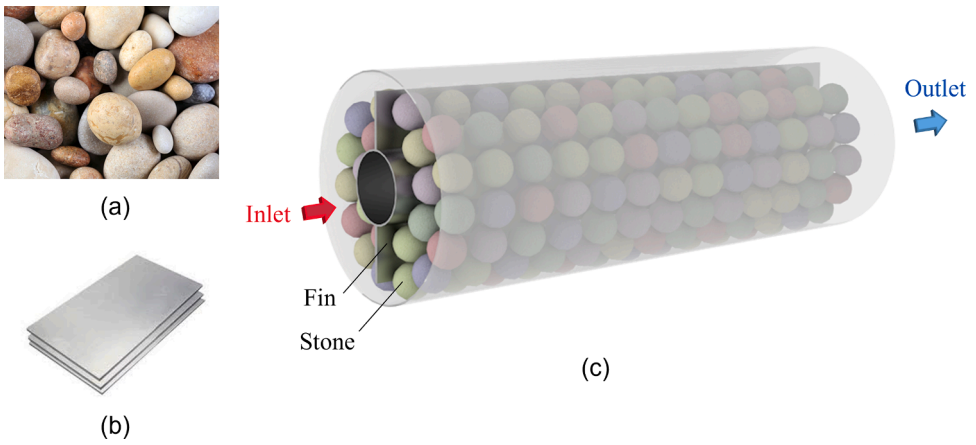

Fig. 1. Photograph of (a) natural stones and (b) fins; (c) schematic of the fin-stone hybrid structure enhancing heat transfer in a shell-and-tube heat storage unit.

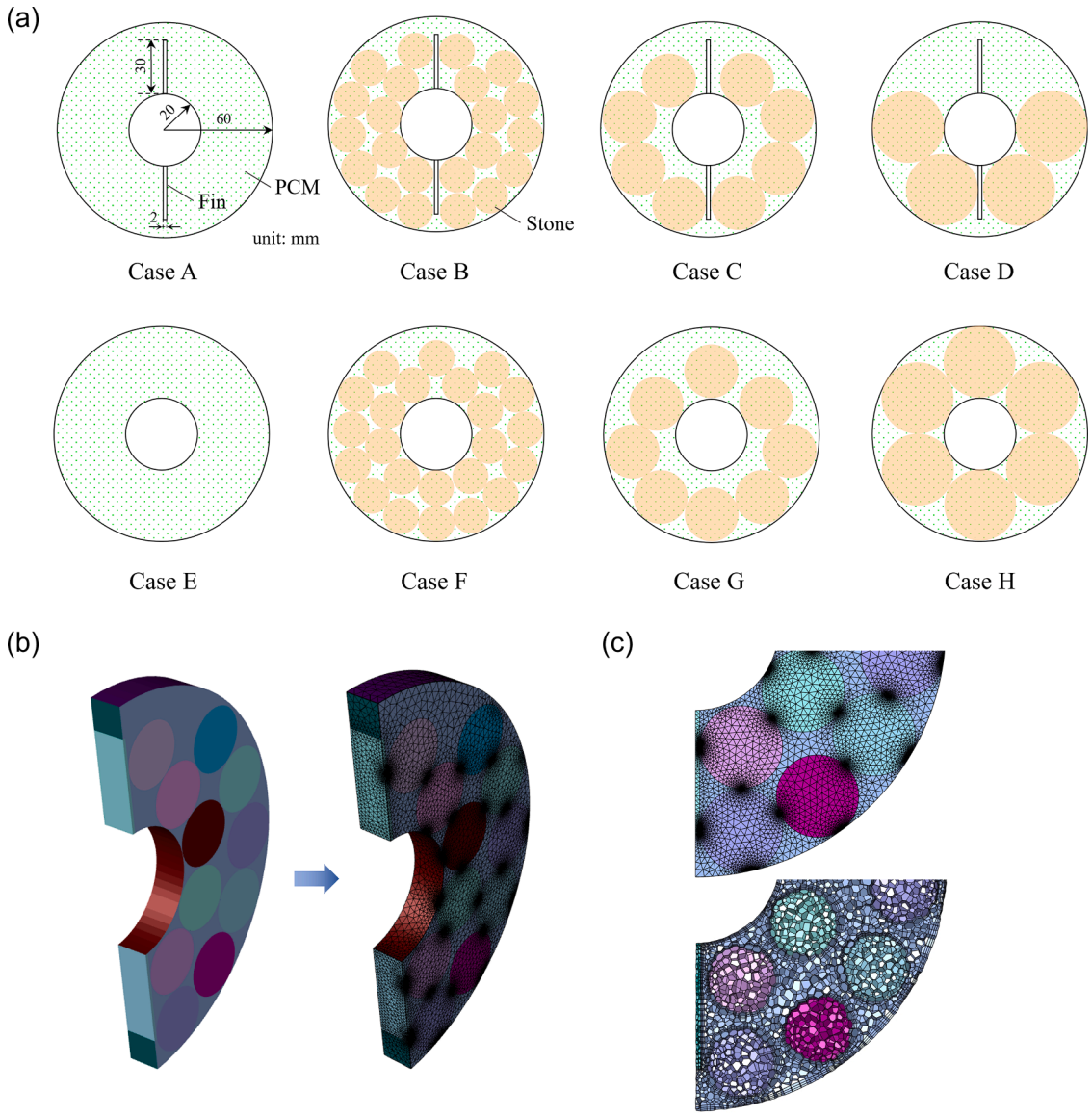

Fig. 2. Schematic of (a) eight cases evaluated in this study, (b) meshing of the physical model, (c) surface and volume meshes.

Table 1
Settings of eight cases evaluated in this study (L_{unit}, H_{fin}, τ_{fin}, D_{stone}, N_{stone}, and ε are the length of the heat storage unit, height of fins, thickness of fins, diameter of stones, number of stones, and the volume fraction of the PCM, respectively).

No.	L_{unit}, mm	H_{fin}, mm	τ_{fin}, mm	D_{stone}, mm	N_{stone}, -	ε, -
Case A	40	30	2	–	0	0.99
Case B	20	30	2	20	22	0.53
Case C	30	30	2	30	8	0.61
Case D	40	30	2	40	4	0.65
Case E	40	–	–	–	0	1
Case F	20	–	–	20	23	0.52
Case G	30	–	–	30	8	0.63
Case H	40	–	–	40	6	0.50

Table 2
Properties of paraffin, copper, granite, and water [11,47].

Property	Paraffin	Copper	Granite	Water
Specific heat, J/(kg·K)	2850	380	820	4182
Density, kg/m^3	785	8920	2640	998
Thermal conductivity, W/(m·K)	0.3 (solid)/0.1 (liquid)	401	2.86	0.6
Coefficient of thermal expansion, K^{-1}	3.09×10^{-4}	–	–	–
Latent heat, J/kg	175,240	–	–	–
Melting point, °C	54.4 - 64.1	–	–	–
Viscosity, mPa·s	3.65	–	–	1.00

annular space and the HTF flowing through the inner tube is a popular device for commercial and industrial thermal energy storage applications [44]. In this study, the fin-stone hybrid structure is placed in the annular space, as indicated in Fig. 1, to enhance the heat transfer of the PCM. Natural stones, as shown in Fig. 1(a), are widely accessible and do not need industrial fabrication. Fins, as indicated in Fig. 1(b), can be taken from metal boards and are easy to fabricate. Straight vertical fins are used, so they do not have to withstand the weight of stones, and the hybrid structure is stable. As seen in Fig. 1(c), vertical fins are welded to the inner tube, while stones are placed in the annulus and in contact with fins, forming a fin-stone hybrid structure. The rest of the space of the annulus is filled by the PCM, while the HTF flows in the inner tube. The heat storage unit is horizontally placed, ensuring its stability. The stones' shape is irregular in practice, not cubic, spherical, cylindrical, etc., so it is hard to characterise and reproduce their shapes accurately. The shape of real stones is not exactly spherical, but very close to being spherical, as indicated in Fig. 1(a). And since the stone shapes are diverse, it would be hard to focus on a certain parameter's effect. So, in this study, stones are assumed spherical, and their equivalent size can be represented by the diameter of spheres. The assumption of the spherical shape makes stones have uniform geometry, removing the interference of the diverse shapes, and enables focusing on a certain parameter (the stone size in the current study).

Fig. 2(a) shows eight cases evaluated in this study: the shell-and-tube heat storage units with fins (Case A), with the fin-stone hybrid structure (Cases B-D), without enhancement (Case E), with stones (Cases F-H).

Table 3
Liquid fraction (L_f) and total charging time under different numerical settings.

Number of cells, -	Time step, s	L_f at 5000 s, -	L_f at 10,000 s, -	Total charging time, s
61,532	1	0.5572	0.9194	13,337
84,968	1	0.5597	0.9208	13,314
120,746	1	0.5627	0.9225	13,295
84,968	0.5	0.5589	0.9204	13,322.5
84,968	1	0.5597	0.9208	13,314
84,968	2	0.5609	0.9213	13,300

Table 4
The experimental configurations in Refs. [22,59].

Parameter	Ref. [22]	Ref. [59]
Length of the tube, mm	762, 304.8 (inner, outer)	800, 500, 500 (inner, middle, outer)
Radius of the tube, mm	6.4, 25.4 (inner, outer)	25.4, 75, 100 (inner, middle, outer)
Thickness of the tube, mm	1.7, 1.3 (inner, outer)	1.2, 2, 2 (inner, middle, outer)
Initial temperature, °C	25	93
HTF type	Air	Water
HTF temperature, °C	70, 25 (heating, cooling)	68

Table 5
Material properties in Refs. [22,59].

Property	Ref. [22]	Ref. [59]
Thermal conductivity of PCM, W/(m · K)	0.25	0.2
Specific heat of PCM, J/(kg · K)	2510	2000
Density of PCM, kg/m^3	730–790	950 (solid)/770 (liquid)
Melting temperature of PCM, °C	50–60	77–85
Latent heat of PCM, J/kg	117,000	176,000
Thermal conductivity of the fin, W/(m · K)	–	387.6
Specific heat of the fin, J/(kg · K)	–	381
Density of the fin, kg/m^3	–	8978

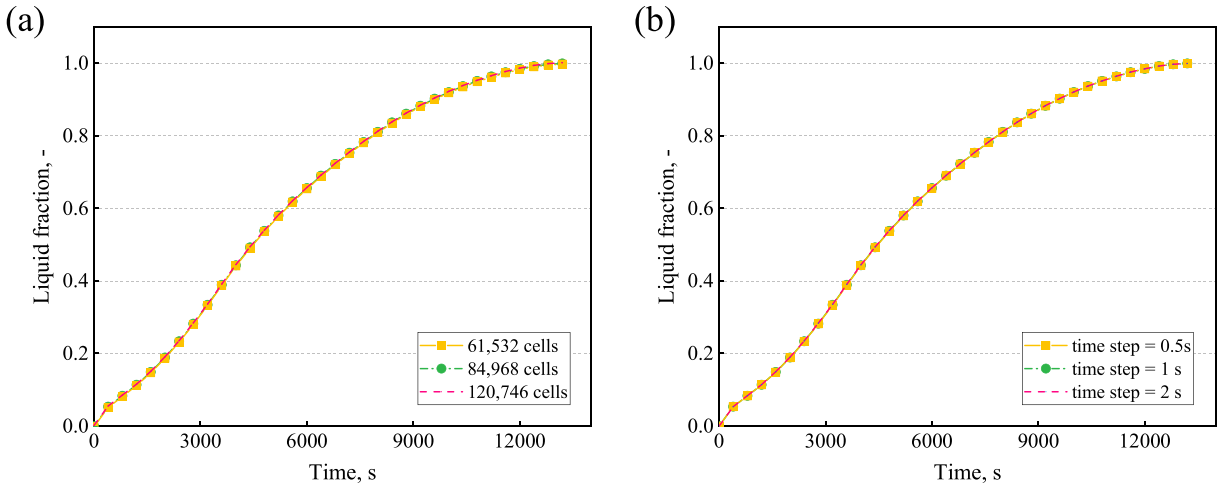

Fig. 3. The effects of (a) grid number and (b) time step on the liquid fraction.

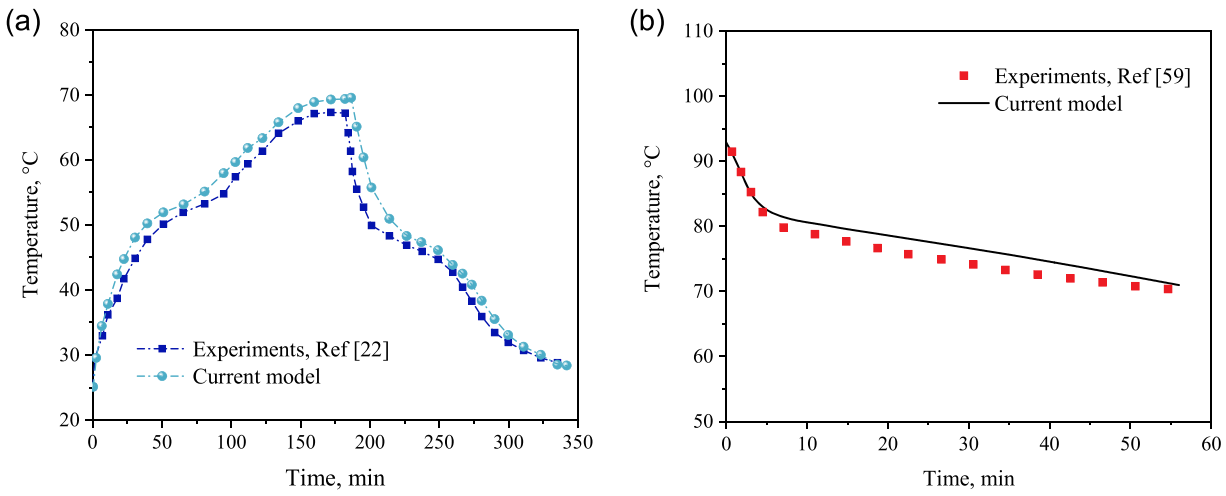

Fig. 4. Model validation with (a) Atal et al.'s and (b) Al-Abidi et al.'s experiments [22,59].

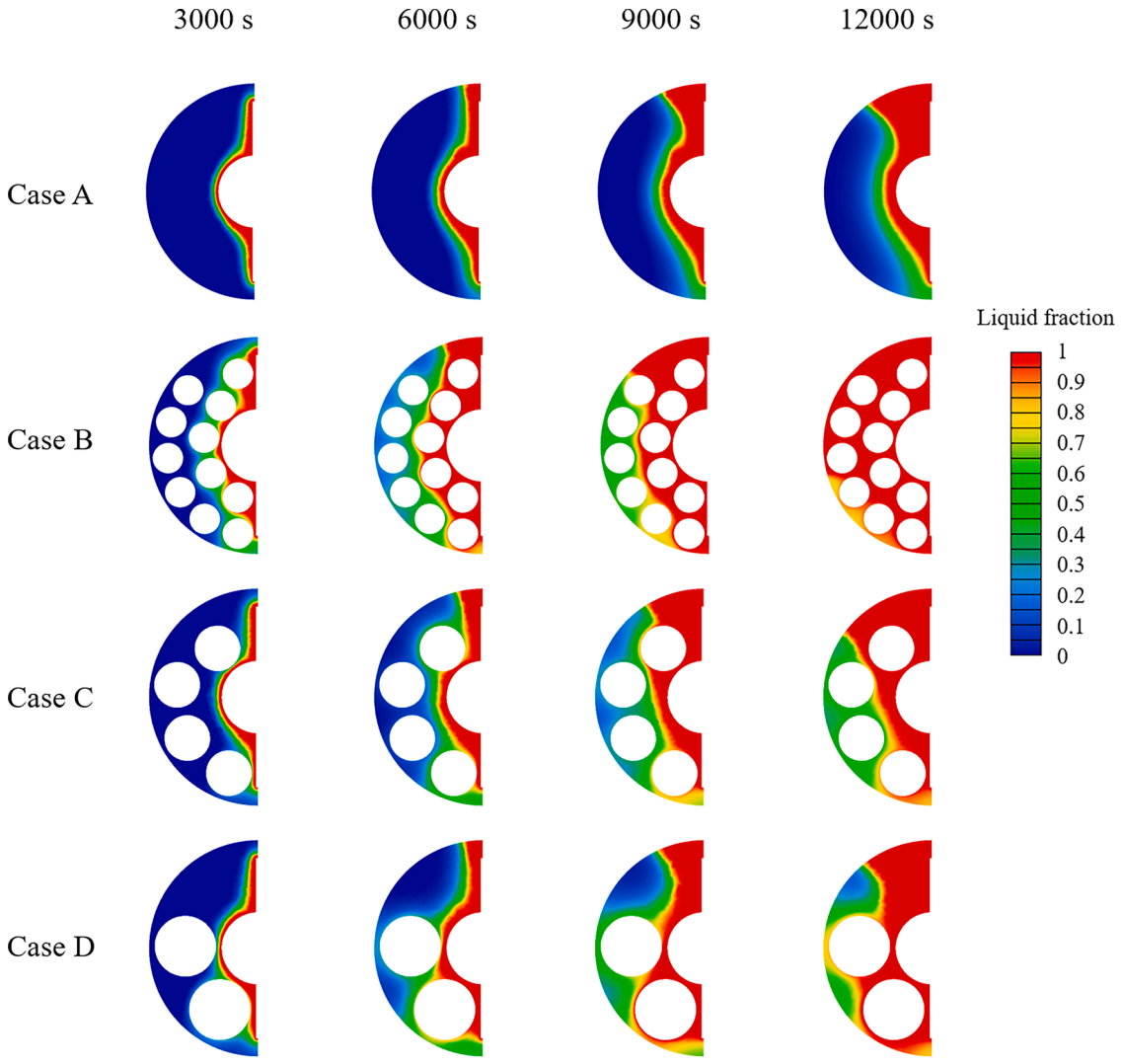

Fig. 5. Melting front propagation of the PCM in Cases A-D.

The outer radii of the heat storage unit and the inner tube are 60 mm and 20 mm, respectively, while the fins are 30 mm high and 2 mm thick; stones are 20 mm, 30 mm, and 40 mm in diameter in Case B, Case C, and Case D, respectively. The high thermal conductivity of copper (the tube material) and the thin wall enable the neglection of the tube thickness [38]. For Case G, the heat storage unit in practice is very long, and the top stone can be approximately assumed in the middle, so the arrangement in Case G should be reasonable and used in this study. The settings of the eight cases are listed in Table 1. The volume fraction of the PCM, ε, is calculated by:

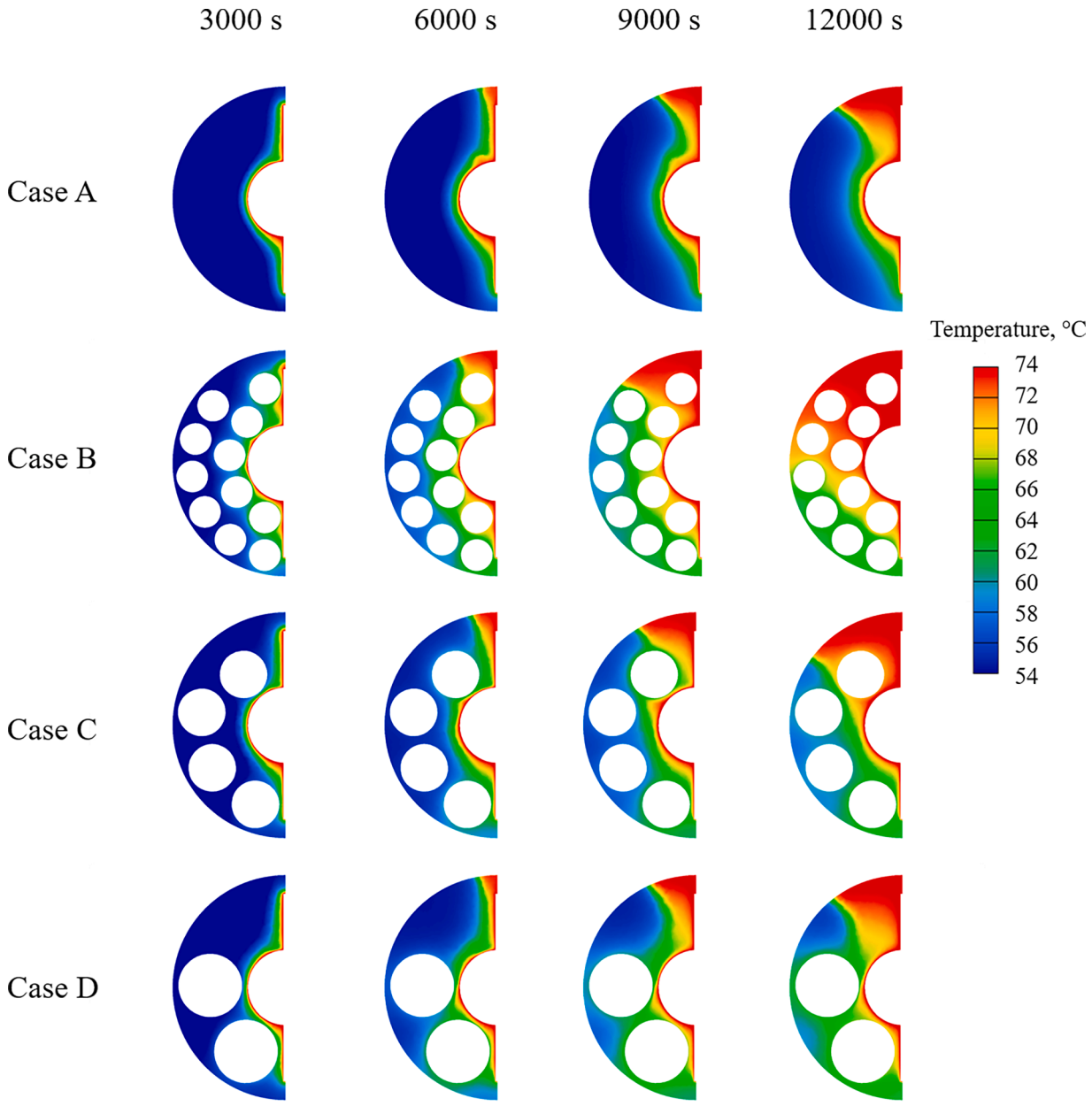

Fig. 6. Temperature fields of the PCM during charging in Cases A-D.

$$\varepsilon = \frac{V_{\text{void}}}{V_{\text{total}}} = \frac{V_{\text{total}} - V_{\text{stone}} - V_{\text{fin}}}{V_{\text{total}}} = 1 - \frac{\frac{\pi d^3}{6}N + 2\omega h l_{\text{u}}}{\frac{\pi\left(D_{\text{shell}}{}^2 - D_{\text{tube}}{}^2\right)}{4} l_{\text{u}}} \quad (1)$$

where V_{void}, V_{stone}, V_{fin}, and V_{total} are the void, stone, fin, and total volumes, respectively; D_{shell} and D_{tube} are the shell and tube diameters, respectively; l_{u} is the length of a single unit, which equals d; ω and h are fin thickness and height, respectively.

A quarter of a unit with one layer of stones is used in this simulation owing to symmetry, as indicated in Fig. 2(b). Then, it is meshed using the Meshing Module of ANSYS Fluent 2021. The extremely small gap between two tangent spheres could lead to computational divergence. The "near-miss" method, which reduces the diameter to 0.99 times [45], is adopted to solve this problem. The skewness of all volume meshes (Fig. 2(c)) is less than 0.78, meeting the requirement of the fluid simulation [46]. Paraffin acts as the PCM, copper fins and granite as thermal enhancers, while water serves as the HTF (Table 2).

2.2. Governing equations

The following assumptions are made for the numerical modelling: (1) stones are spherical, as mentioned above; (2) the PCM, fins and stones are homogeneous and isotropic; (3) the liquid PCM is incompressible; (4) material properties, except for the PCM density, are temperature-independent [48–52]; (5) the Boussinesq approximation deals with natural convection to get a fast convergence [53,54].

The enthalpy-porosity model is used to simulate the phase change of the PCM [55], and the continuity equation is given by:

$$\frac{\partial \rho_{\text{f}}}{\partial t} + \nabla\cdot\left(\rho_{\text{f}}\vec{\text{U}}\right) = 0 \quad (2)$$

Since the fluid is assumed incompressible, this equation reduces to:

$$\nabla\cdot\vec{\text{U}} = 0 \quad (3)$$

The momentum equations are given by [56]:

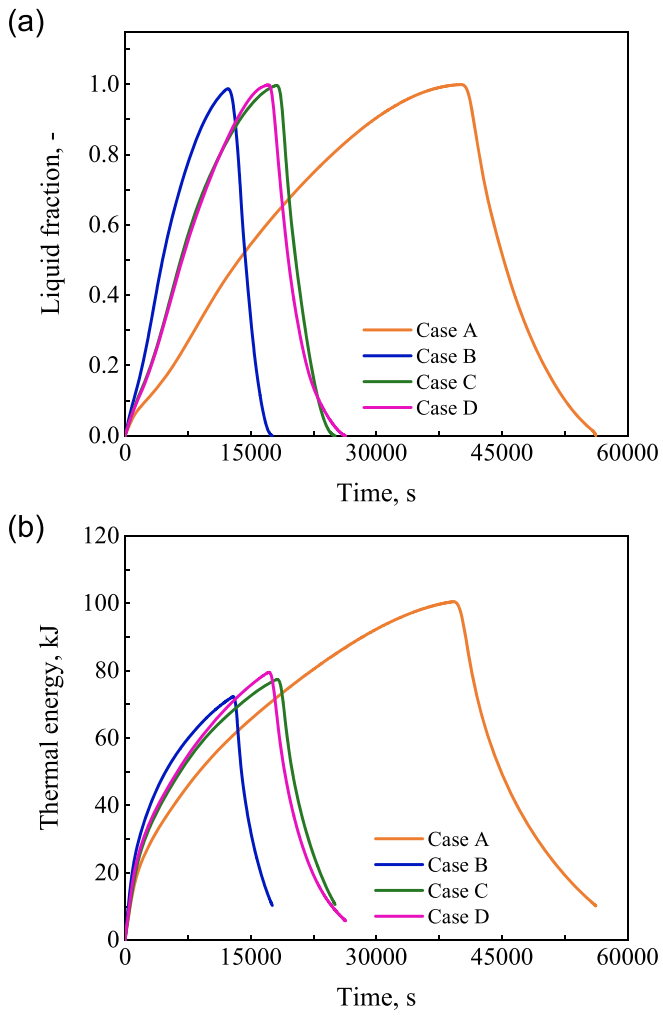

Fig. 7. (a) Volume change of the liquid PCM in Cases A-D; (b) variation of thermal energy with time in Cases A-D.

$$\rho_{\mathrm{PCM}}\frac{\partial \mathrm{u}}{\partial \mathrm{t}}+\rho_{\mathrm{PCM}}\left(\vec{\mathrm{U}}\cdot\nabla \mathrm{u}\right)=-\frac{\partial \mathrm{p}}{\partial \mathrm{x}}+\mu_{\mathrm{PCM}}\nabla^2\mathrm{u}-\frac{(1-\varphi)^2}{(\varphi^3+\omega)}\mathrm{A}_{\mathrm{mushy}}\mathrm{u} \tag{4}$$

$$\rho_{\mathrm{PCM}}\frac{\partial \mathrm{v}}{\partial \mathrm{t}}+\rho_{\mathrm{PCM}}\left(\vec{\mathrm{U}}\cdot\nabla \mathrm{v}\right)=-\frac{\partial \mathrm{p}}{\partial \mathrm{y}}+\mu_{\mathrm{PCM}}\nabla^2\mathrm{v}+\rho_{\mathrm{PCM}}\,\mathrm{g}\,\beta\left(\mathrm{T}-\mathrm{T}_{\mathrm{m,\ s}}\right)-\frac{(1-\varphi)^2}{(\varphi^3+\omega)}\mathrm{A}_{\mathrm{mushy}}\mathrm{v} \tag{5}$$

$$\rho_{\mathrm{PCM}}\frac{\partial \mathrm{w}}{\partial \mathrm{t}}+\rho_{\mathrm{PCM}}\left(\vec{\mathrm{U}}\cdot\nabla \mathrm{w}\right)=-\frac{\partial \mathrm{p}}{\partial \mathrm{z}}+\mu_{\mathrm{PCM}}\nabla^2\mathrm{w}-\frac{(1-\varphi)^2}{(\varphi^3+\omega)}\mathrm{A}_{\mathrm{mushy}}\mathrm{w} \tag{6}$$

where ρ is the material density; the subscript f referes to the fluid (liquid PCM or HTF); U is the velocity vector where u, v, and w are the components in the x, y, and z directions, respectively. g, T, and p are the gravitational acceleration, temperature, and pressure, respectively. β is the thermal expansion coefficient, and μ is the PCM viscosity. A_{mushy} is the mushy zone constant (10^7) [19]. ω is a small number, which is set as 0.001, to avoid being divided by zero [57]. The third term on the right side of Eq. (5) denotes the Boussinesq approximation considering the effect of the buoyancy force. The last terms in Eqs. (4)–(6) are the damping terms [58].

φ, the liquid fraction in a single cell, is predicted by [56]:

$$\varphi=\begin{cases}0 & T<T_{\mathrm{m,\ s}}\\ \dfrac{T-T_{\mathrm{m,\ s}}}{T_{\mathrm{m,\ l}}-T_{\mathrm{m,\ s}}} & T_{\mathrm{m,\ s}}\le T\le T_{\mathrm{m,\ l}}\\ 1 & T>T_{\mathrm{m,\ l}}\end{cases} \tag{7}$$

where $T_{\mathrm{m,\ s}}$ and $T_{\mathrm{m,\ l}}$ is the PCM solidus and liquidus temperatures, respectively.

The energy equation of the PCM is

$$\rho_{\mathrm{PCM}}\,c_{\mathrm{p,\ PCM}}\left(\frac{\partial \mathrm{T}}{\partial \mathrm{t}}+\vec{\mathrm{U}}\cdot\nabla \mathrm{T}\right)=\mathrm{k}_{\mathrm{PCM}}\nabla^2\mathrm{T}-\rho_{\mathrm{PCM}}\mathrm{L}\frac{\mathrm{d}\varphi}{\mathrm{dt}} \tag{8}$$

where c_{p}, L, and k are the specific heat, latent heat, and thermal conductivity, respectively.

Forced convection takes place in the HTF, and the continuity, momentum, and energy equations are given by [24]:

$$\nabla\cdot\vec{\mathrm{U}}=0 \tag{9}$$

$$\rho_{\mathrm{HTF}}\frac{\partial \vec{\mathrm{U}}}{\partial \mathrm{t}}+\rho_{\mathrm{HTF}}\left(\vec{\mathrm{U}}\cdot\nabla\right)\vec{\mathrm{U}}=-\nabla \mathrm{p}+\mu_{\mathrm{HTF}}\nabla^2\vec{\mathrm{U}} \tag{10}$$

$$\rho_{\mathrm{HTF}}\,c_{\mathrm{p,HTF}}\frac{\partial \mathrm{T}}{\partial \mathrm{t}}+\rho_{\mathrm{HTF}}\,c_{\mathrm{p,\ HTF}}\,\vec{\mathrm{U}}\cdot\nabla \mathrm{T}=\mathrm{k}_{\mathrm{HTF}}\nabla^2\mathrm{T} \tag{11}$$

Heat conductions occurs in fins and stones, and energy equations are

$$\rho_{\mathrm{fin}}\,c_{\mathrm{p,\ fin}}\frac{\partial T}{\partial t}=k_{\mathrm{fin}}\nabla^2T \tag{12}$$

$$\rho_{\mathrm{stone}}\,c_{\mathrm{p,\ stone}}\frac{\partial T}{\partial t}=k_{\mathrm{stone}}\nabla^2T \tag{13}$$

2.3. Initial and boundary conditions

Initial conditions:

$$T\ (t=0)=T_{\mathrm{ini}} \tag{14}$$

where T_{ini} is the initial temperature, equal to the ambient temperature (23 °C).

Boundary conditions:

$$\left.\frac{\partial T}{\partial \vec{n}}\right|_{\Omega}=0 \tag{15}$$

where Ω denotes the outer surface of the heat storage unit.

For the HTF:

$$Q_{\mathrm{HTF}}=constant \tag{16}$$

$$T_{\mathrm{HTF}}=\begin{cases}T_{\mathrm{hot}}, & \text{charging}\\ T_{\mathrm{cold}}, & \text{discharging}\end{cases} \tag{17}$$

where Q_{HTF} is the flow rate of the HTF, which is 4 L/min; T_{HTF} is the inlet temperature of the HTF, which is set as 75 °C (T_{hot}) during charging and 23 °C (T_{cold}) during discharging. These values are set because the potential application of the fin-stone enhanced heat storage unit is waste

Table 6
Charging, discharging, and total time in different cases.

No.	Case A	Case B	Case C	Case D	Case E	Case F	Case G	Case H
Charging time, s	40,584	13,314	18,819	17,837	92,490	23,122	36,973	23,578
Discharging time, s	15,620	4262	6263	8487	19,406	6458	8448	5842
Total time, s	56,204	17,576	25,082	26,324	111,896	29,580	45,421	29,420

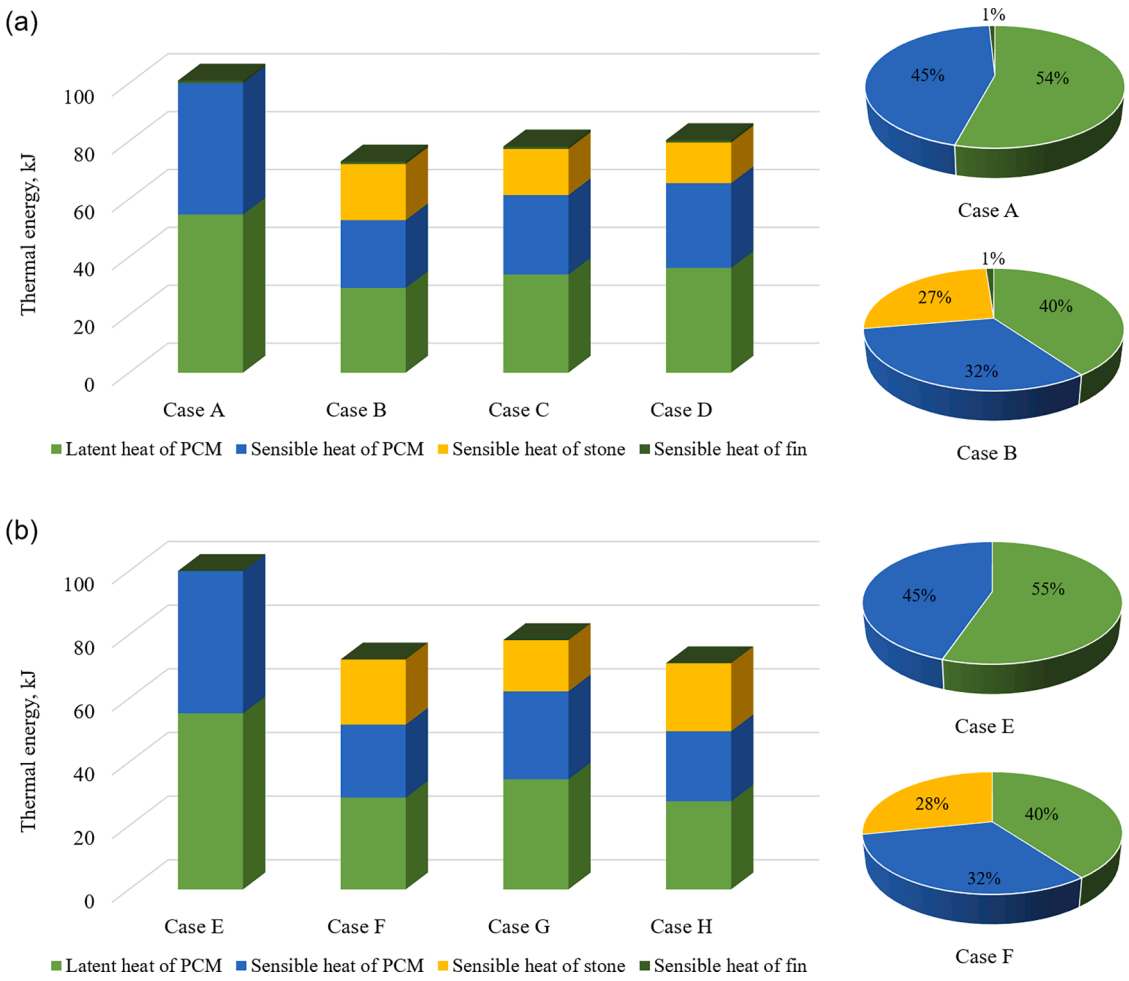

Fig. 8. Components of thermal energy in (a) Cases A-D and (b) Cases E-H (latent heat and sensible heat herein refer to latent heat thermal energy and sensible heat thermal energy, respectively).

heat recovery from the data centre for residential use: the HTF from the data centre is about 75 °C with a velocity of 0.05 m/s [54], i.e. the volume rate of 4 L/min in the current inner tube; the HTF from the residential building is at the ambient temperature (23 °C).

2.4. Independence test of grid and time step

ANSYS Fluent 2021 was used to solve the numerical model. The continuity, momentum, and energy equations are discretised using the finite volume method (FVM), and the convergence criteria are 10^{-4}, 10^{-4}, and 10^{-6}, respectively. The pressure and velocity are coupled with the SIMPLE scheme, while the under-relaxation factors of pressure, density, body forces, momentum, liquid fraction update, and energy are 0.3, 1, 1, 0.7, 0.9, and 1, respectively.

Case B was employed to test the grid and time step independence, where three mesh sets (61,532 cells, 84,968 cells, and 120,746 cells) and time steps (0.5 s, 1 s, and 2 s) were included. As Fig. 3 and Table 3 shows, the average liquid fraction of the PCM (L_f) differs insignificantly between different mesh sets, and the deviation in the total charging time under different time steps is less than 0.17%. Therefore, the 84,968 cells and 1 s were used in this study.

2.5. Model validation

The numerical model is validated from two aspects, where the first one is the validation of the Melting/Solidification model, and the second one is the validation of the fin-stone/PCM configuration. The first validation is carried out by comparing the paraffin temperature at the midpoint of a shell-and-tube heat storage unit in Atal et al.'s experiments [22]. The detailed experimental configurations and material properties are listed in Tables 4 and 5. From Fig. 4(a), the average difference between the numerical results predicted by the current model and experimental data is 2.2 °C, which may be attributed to the completely adiabatic boundary leading to slightly higher temperatures in the simulation. The average relative deviation in the temperature is 4.6%, with a maximum deviation of 17.8% and a minimum deviation of 0.6%. The trend of the paraffin temperature in the simulation is consistent with that in the experiment, and the temperature is nearly identical to the experimental data at the final stage, verifying the Melting/Solidification model.

Since the fin-stone/PCM configuration is a novel structure, there is little experimental data available in the open reports. The principle of the fin-stone hybrid structure is similar to fins, which enhances heat transfer by extending the contact area; as a consequence, the coupled boundary between thermal enhancers and PCM is included in the numerical model. The experimental results of a finned unit [59] are used to validate the fin-stone/PCM configuration, and this strategy has been justified in our previous research [57]. Fig. 4(b) presents the average temperature by fifteen thermocouples in a shell-and-tube unit with internal and external fins. The average difference between numerical and experimental results is 1.8 °C; the maximum relative deviation is lower than 5%, and the average deviation over the discharging is 2.4%. The deviation is within the acceptable range, indicating the numerical model is reliable and accurate enough to support the following results.

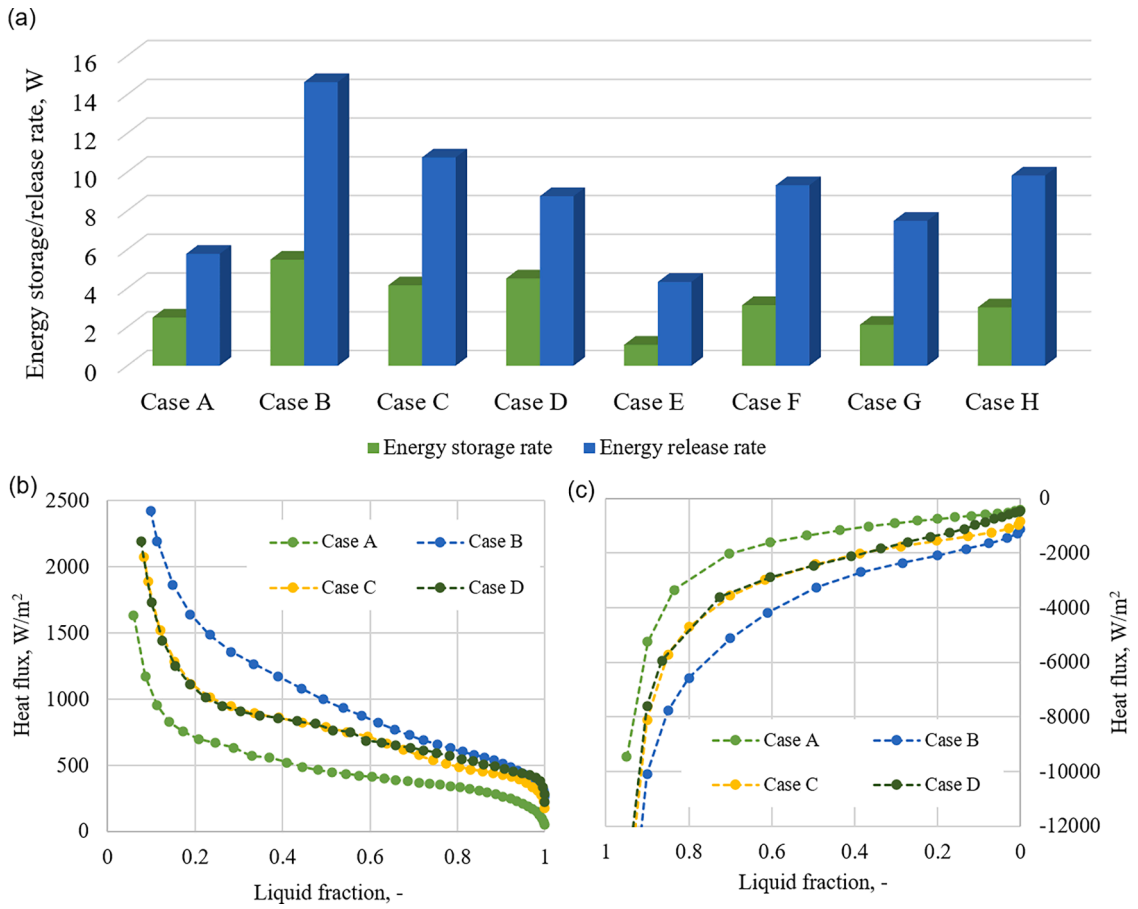

Fig. 9. (a) Energy storage and release rates of different cases; heat flux of the inner tube in (b) charging and (c) discharging.

3. Results and discussions

3.1. Comparison between the hybrid structure with fins

Fins are a popular structure that enhances the heat transfer of the PCM in a shell-and-tube heat storage unit. The novel hybrid structure is first compared with traditional fins to demonstrate its effect. The melting front of the PCM at the plane of half the thickness is captured, as illustrated in Fig. A1. The melting front propagation and temperature fields of the PCM in Cases A-D during charging are presented in Fig. 5 and Fig. 6, respectively.

At the time of 3000 s, the PCM near the tube and fins are melted first in all cases owing to the high temperature of the tube and high thermal conductivity of copper. Moreover, the liquid areas ($\varphi = 1$) in Case A, Case C, and Case D are almost identical, indicating 30 mm- and 40 mm-sized stones have little effect at this stage. The mushy zone in Case B is relatively larger probably because the stone size is small, and the heat from the tube and fins can penetrate stones easily.

At 6000 s, the solid-liquid interface in Case A is almost parallel to that at 3000 s, suggesting heat conduction is the primary heat transfer mode. Case C and Case D have similar phase fields where the PCM near the tube and fins are melted fully, the part surrounding stones in contact with the tube and fins is mushy, and the rest is solid. In comparison, the melting front propagation in Case B is obviously faster: not only the liquid region is extended, but also almost all the rest of PCM is mushy. Moreover, the PCM layer around stones in contact with the tube and fins is melted fully owing to the fast heat conduction induced by the small stone size, and the part around other stones is mushy since the thermal conductivity of stones is much higher than that of the PCM (2.86 W/m/K of granite versus 0.3 W/m/K of solid paraffin).

As the charging proceeds, at 9000 s, the solid-liquid interface in Case A is slightly deformed since natural convection makes a difference to the melting. A similar melting front can be observed in Case C, where the PCM on the left side is mushy in comparison with the solid PCM in Case A. The PCM in the lower half of Case D is fully melted or highly mushy, while the PCM at the top-left corner is solid because of the low thermal conductivity of paraffin and no thermal enhancement structures. The melting rate in Case B is the highest, especially for the PCM on the left side, which is highly mushy in comparison with the solid PCM in other cases. That is because the volume fraction of stones is high (0.47 in Case B versus 0.39 in Case C versus 0.35 in Case D), and the surface area is large owing to the small stone size.

Most PCM has been melted fully in Case B, and the average liquid fraction (L_f) reaches 0.98 at 12,000 s, as shown in Fig. 7(a). The only mushy PCM is located at the bottom left corner, where heat conduction and natural convection are difficult to exert an effect. The PCM at the bottom of Case C and Case D melted faster than that at the left side because the fin and stone at the bottom extend the contact area between the PCM and heat source and have high thermal conductivity, which promotes heat conduction and natural convection. The liquid fraction in Case C and Case D is similar, which is 0.83 and 0.84, respectively. The melting area at the top of Case A is large, indicating the melting rate is faster because of natural convection. In comparison, the PCM on the left side is still solid caused by the poor heat transfer performance. The liquid fraction in Case A is the lowest, which is only 0.45 at 12,000 s.

The charging time in the four cases is 40,584 s, 13,314 s, 18,819 s, and 17,837 s, respectively, as listed in Table 6, meaning the fin-stone hybrid structure decreases the charging time by 67%, 54%, and 56% compared to fins. Considering the decreased volume of the PCM, the melting rate is increased by 63%, 34%, and 51% in Case B, Case C, and Case D, respectively. It can be concluded that the fin-stone hybrid structure can accelerate the phase change of the PCM, and Case B with

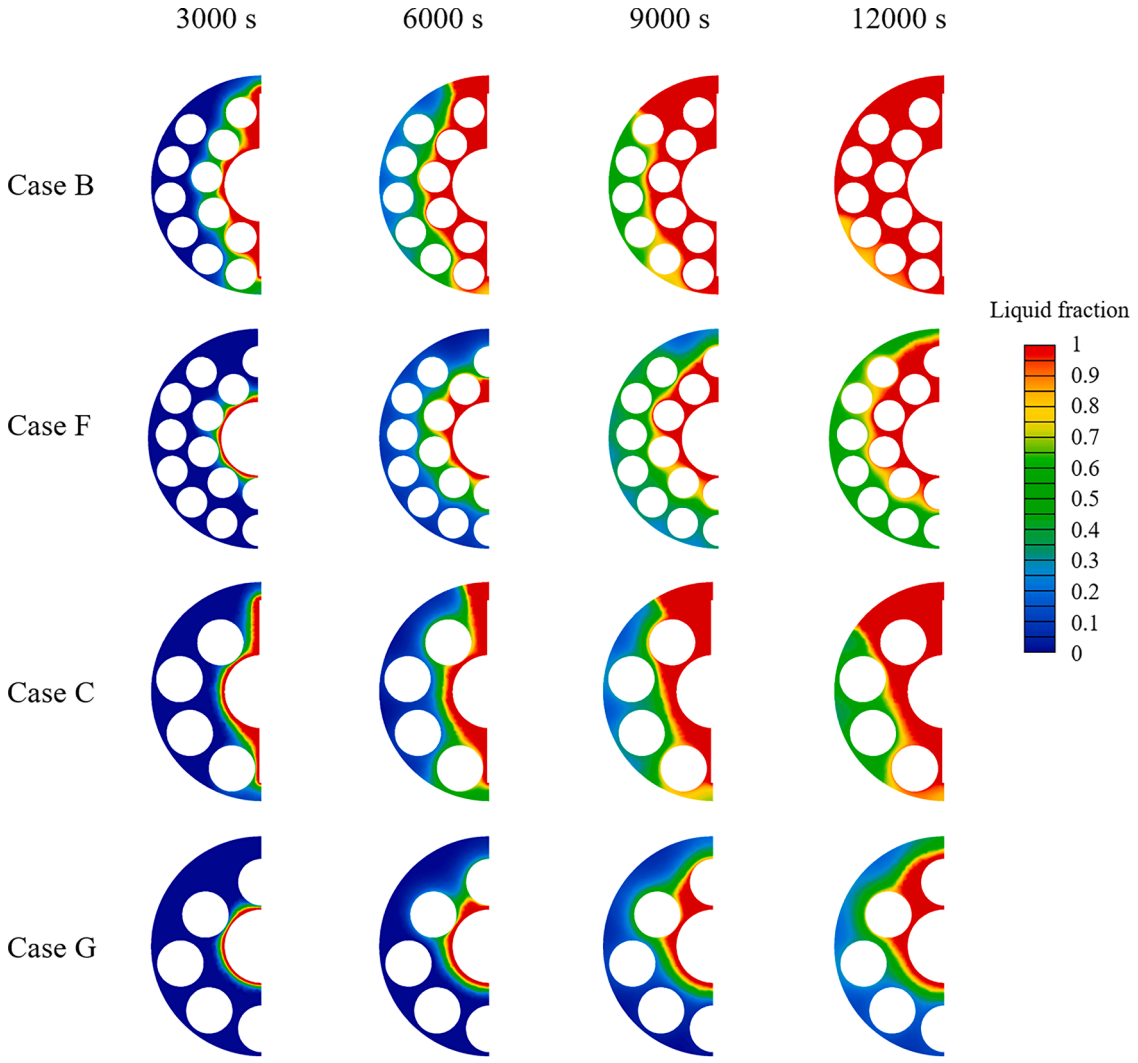

Fig. 10. Comparison of the melting front between different cases.

20 mm-sized stones has the highest melting rate.

Fig. 6 demonstrates the temperature fields of the four cases, where the isotherms in Case A are almost parallel to the tube and fins at 3000 s, as heat transfer is dominated by heat conduction. Case C and Case D show similar temperature fields, meaning the effect of 30 mm- and 40mm-sized stones is negligible at this moment, while Case B presents a zigzag-shaped high-temperature isotherm probably because more stones are in contact with the tube and fins, which is beneficial to conducting their heat.

At the time of 6000 s, the distinction between high- and low-temperature regions in Case A is clear, with a maximum temperature difference of 27 °C, though the melting front moves forward. By contrast, Case B has a relatively uniform temperature field where the PCM is about 66 °C around stones close to the tube and 57 °C on the left side. The temperature fields of Cases C and D are like Case A to a certain extent, with cold PCM on the left side.

At 9000 s, the high temperature in Case A is located around the tube and fins as well as at the top caused by natural convection, while the PCM on the left side is still low temperature attributed to weak heat conduction by the low thermal conductivity. The temperature of the PCM on the left side of Case B is obviously higher than that in Case A, and the maximum temperature difference is 16.5 °C, lower than 19.3 °C in Case C and 20.3 °C in Case D.

As the charging proceeds, at 12,000 s, the high-temperature region is extended in Case A, while the PCM on the left side is still low temperature. For Case B, the temperature generally decreases from top to bottom because the hot PCM flows to the top under the buoyancy force, and the cold PCM flows to the bottom due to the density difference. There is a clear boundary, i.e., the 68 °C isotherm, observed in Case C where the PCM at the top right is high temperature due to natural convection and heat conduction by the stone, while the PCM at the bottom left is relatively low temperature perhaps because the left two stones are not in direct contact with the tube and fins. Case D has two stones at the lower and in contact with the tube; therefore, the temperature of the PCM around these stones is high. The PCM at the top left is low temperature as a result of natural convection and no heat transfer enhancement structures. The maximum temperature difference in the four cases is 20.6 °C, 13.7 °C, 17.5 °C, and 19.1 °C, respectively.

From Fig. 7(b), where thermal energy is calculated based on a heat storage unit of 40 mm length, different structures demonstrate different performances. The detailed equations to calculate various energy storage parameters are provided in Appendix B. The fin-stone hybrid structures accelerate charging and discharging while lowering energy storage capacity. Specifically, Case B shows the shortest total charging and discharging time, saving 69% compared with Case A; meanwhile, it has the least total thermal energy, 28% lower than Case A. It is noticeable that the volume fraction of the PCM in Case B is 0.53, 46% lower than 0.99 in Case A. The decrease in the total energy is less significant than the decrease in the volume fraction of the PCM because stones can store 27% of total thermal energy, as indicated in Fig. 7(a), suggesting

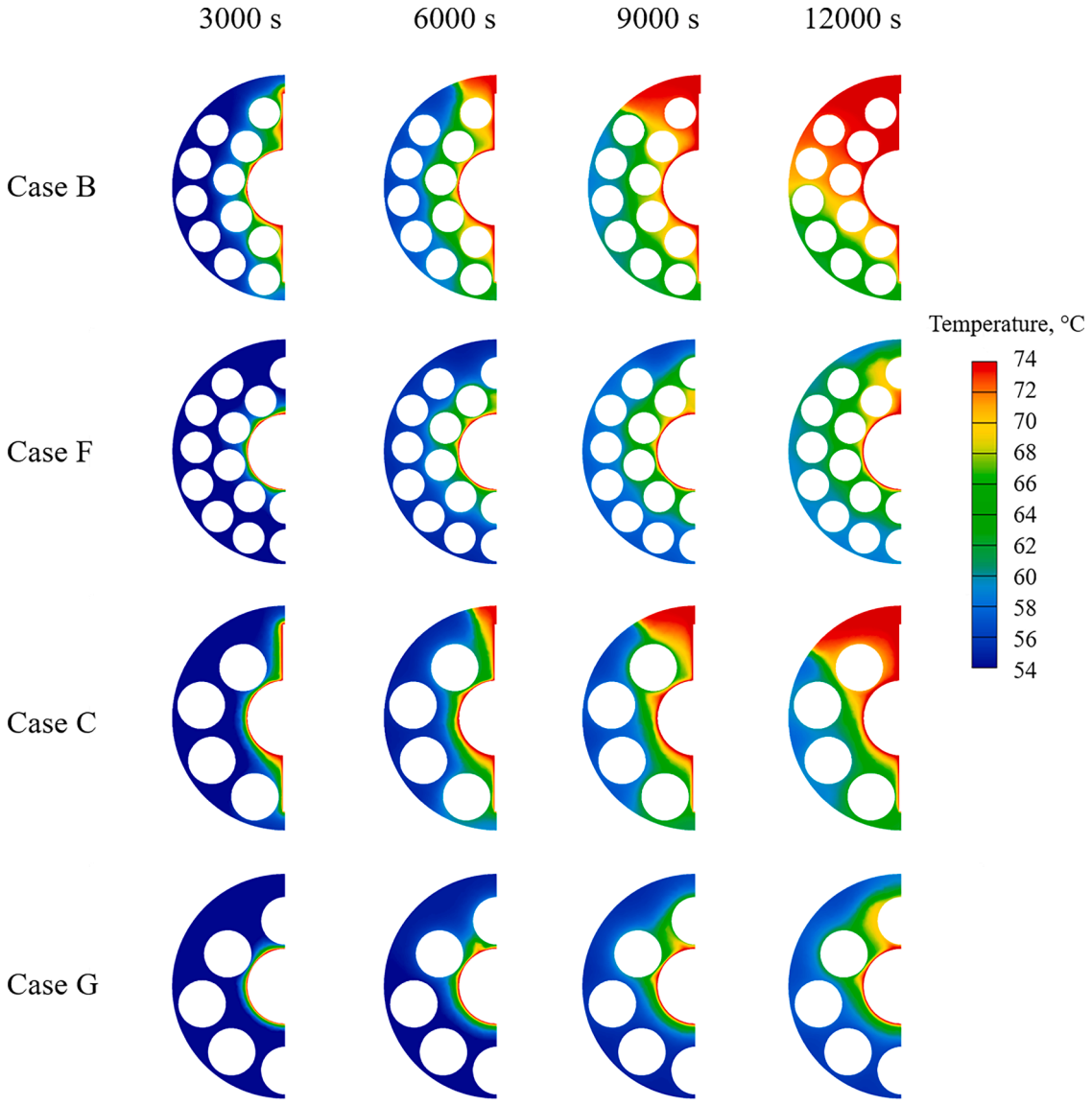

Fig. 11. Comparison of the temperature field between different cases.

that stones are not only thermal enhancers but also energy storage media. Fins only store 1% of total thermal energy since they mainly serve as thermal enhancers.

Case D is superior to Case C in charging owing to the faster energy storage rate and higher energy storage capacity; however, its discharging lasts longer, probably caused by fewer stones leading to a relatively weak heat conduction. The decrease in the discharging time in Case C and Case D is significant, 60% and 46% less than in Case A, respectively, while the total time is 55% and 53% less.

Considering the different PCM volumes and the time decrease, the energy storage and release rates are calculated, as presented in Fig. 9(a). Case B has the highest energy storage rate, 120% higher than Case A, followed by Case D and Case C, which are 81% and 67% higher, respectively. Case B has the most stones whose volume fraction is 0.47, and the stone size is small, leading to a large surface area. Moreover, many stones are in contact with the tube and fins, which is beneficial for conducting their heat. As a result, the heat flux of the inner tube is the highest, as indicated in Fig. 9(b), which means this structure can absorb and utilise the HTF's heat best. In addition, the heat flux in discharging is also the highest (the absolute value), suggesting this structure can release heat to the HTF best; thus, the energy release rate is the highest amongst the four cases.

The energy storage rate of Case D is slightly higher than that of Case C, perhaps because all stones are at the lower and in contact with the tube, so natural convection is suppressed insignificantly, and heat conduction is stronger. However, its energy release rate is lower than that of Case C, and the possible reason is that Case C has more stones, and heat conduction is the primary heat transfer mode in discharging.

3.2. Comparison between the hybrid structure and stones

The fin-stone hybrid structure is compared with fins in the above section. It is also compared with stones, and the results on the melting front and temperature field are shown in Figs. 10 and 11, respectively. Since Case B and Case F, Case C and Case G have similar volume fractions of the PCM, they are used for comparison. From Fig. 10, there is little difference in the PCM on the left side between Case B and Case F, which are in solid state at 3000 s. The PCM around the fins is fully melted in Case B owing to the strong heat conduction of the fins, while the PCM at the same location in Case F is almost solid. At the time of 6000 s, the solid-liquid interface in Case F is generally annular, indicating heat conduction is the primary heat transfer mode; in comparison, the solid-liquid interface in Case B is distorted due to heat conduction of fins and natural convection. As the melting proceeds

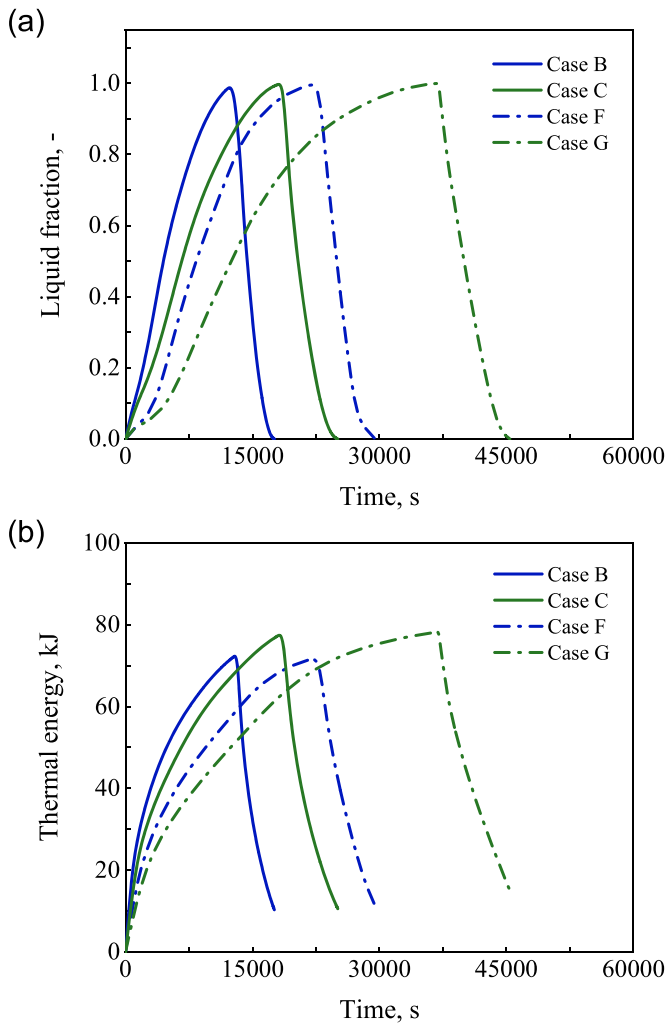

Fig. 12. Variation of (a) liquid fraction and (b) thermal energy in four different cases.

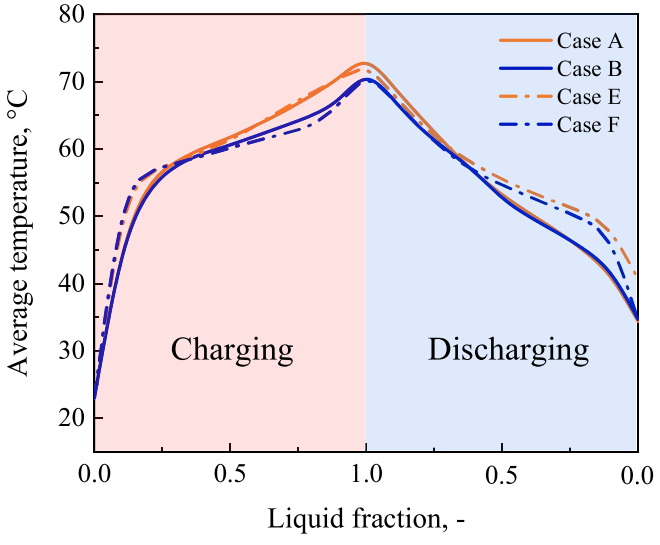

Fig. 13. The variation of the average temperature in four cases during charging and discharging.

Table 7
Comparison of the temperature stability in different cases (ΔT is the temperature change).

No.	ΔT in charging	Compared with Case E	ΔT in discharging	Compared with Case E
Case A	51.1 °C	+ 1.2 °C	39.7 °C	+ 7.4 °C
Case B	48.9 °C	- 1.0 °C	37.2 °C	+ 4.9 °C
Case E	49.9 °C	0	32.3 °C	0
Case F	48.7 °C	- 1.2 °C	37.2 °C	+ 4.9 °C

(9000 s), the natural convection in Case F gets stronger, and there are more PCM melted in the upper, with mushy PCM at the bottom in comparison with the liquid PCM in Case B. At 12,000 s, most PCM has been melted fully in Case B with a little mushy PCM left at the bottom left. By contrast, over half of PCM is still mushy in Case F, especially the part at the bottom where the temperature is low caused by the high density of the cold PCM. The results in Fig. 10 indicate the melting rate in Case B is faster than in Case F, meaning the fin-stone hybrid has stronger heat transfer enhancement than stones. Specifically, the charging time in Case B is 44% shorter than in Case F, while the discharging time is 30% shorter, as shown in Fig. 12(a).

For Case C and Case G, the difference in the melting front at 3000 s and 6000 s mainly lies around fins caused by its heat transfer enhancement. At 9000 s, the PCM at the top of Case C is highly melted owing to the coordination of heat conduction and natural convection, while the PCM only around the tube and the top stone of Case G is highly melted as heat conduction is the primary heat transfer mode. At the time of 12,000 s, the liquid fraction of the PCM around the bottom stone is high in Case C; in comparison, the PCM at the bottom of Case G is hardly melted, perhaps because the bottom stone is not in contact with the tube and fin, so it is hard to conduct the heat from the HTF. As a result, more time is required for charging in Case G, which is 97% longer than in Case C.

Although the temperature fields on the left side of Case B and Case F are nearly identical at 3000 s, the temperature in the middle of Case B is obviously higher than in Case F owing to stronger heat conduction and natural convection by fins. Isotherms in Case F are generally circular at 6000 s, suggesting heat conduction dominates the heat transfer. As the time elapsed (9000 s) and stronger natural convection, the isotherms in the upper extend faster than in the lower. By contrast, in Case B, the isotherms in the upper develop faster from 6000 s, probably because there are more liquid PCMs, as indicated in Fig. 12(a). At the time of 12,000 s, the temperature difference between the upper and lower is significant in Case B, while it is less significant in Case F. In addition, the maximum temperature difference in Case B is 13.7 °C, in comparison with 16.6 °C in Case F, suggesting the fin-stone hybrid structure makes the temperature distribution more uniform. It is seen from Figs. 8 and 12 that Case B and Case F store identical amounts of thermal energy, and the proportion of each thermal energy component is nearly the same. Although fins store only 1% of the total thermal energy in Case B, the fin-stone hybrid structure accelerates thermal energy storage significantly, with 75% higher energy storage rate and 57% higher energy release rate than in Case F.

The difference in the temperature field between Case C and Case G lies around the fins at 3000 s and becomes more significant at 6000 s. And since the bottom stone is in contact with the fin and conducts the heat, the PCM around it has a higher temperature in Case C. At 9000 s, the temperature fields around the tube in the two cases are similar, while the temperature at the top of Case C is significantly higher than in Case G owing to stronger heat conduction and natural convection caused by the fin. The temperature in the upper in both cases develops significantly from 9000 s to 12,000 s; the temperature in the lower of Case C also increases, while that in Case G hardly changes, perhaps because the

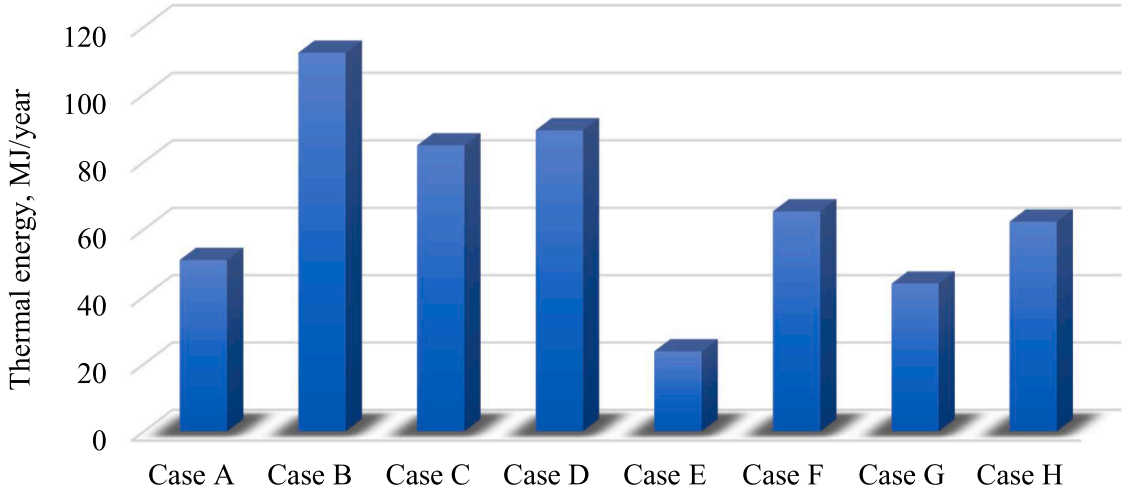

Fig. 14. The yearly energy supplied by different cases.

Table 8
Mass of the eight cases.

No.	Case A	Case B	Case C	Case D	Case E	Case F	Case G	Case H
Mass, kg	0.36	0.70	0.63	0.60	0.32	0.67	0.60	0.69

thermal conductivity of paraffin is low, leading to weak heat conduction.

As shown in Fig. 12(b), Case C has shorter charging and discharging times than Case G, 50% and 23% shorter, respectively. From Fig. 9(a), energy storage and release rates in Case C are 96% and 44% higher than in Case G, respectively. These results, along with those from Case B and Case F, indicate that the fin-stone hybrid structure has better heat transfer enhancement in charging than in discharging, probably because fins are vertical and do not restrict the fluid flow; in charging, fins enhance heat conduction and natural convection, both of which play an important role in heat transfer; in discharging, fins mainly enhance heat conduction which is the primary heat transfer mode, so the enhancement is limited.

3.3. Performance evaluation

One of the advantages of latent heat thermal energy storage is temperature stability during charging and discharging, which is beneficial to stabilise the HTF outlet temperature. This performance is evaluated in the current section. Cases A, B, E, and F are selected because they are representative and cover various configurations, including fins only, the fin-stone hybrid structure, no heat transfer enhancement, and stones only. The average temperature of energy storage media, including the PCM, stones, and fins, in each case, is calculated, and the results are presented in Fig. 13 and Table 7.

For charging, the initial average temperature in all cases is 23.0 °C, and the final average temperature in Case E, where there is no heat transfer enhancement structure, is 72.9 °C, suggesting that the average temperature change is 49.9 °C. The final average temperature in Case A is slightly higher, 74.1 °C, perhaps because the high temperature of fins increases the average temperature. Case B has a low final temperature (71.9 °C) and a relatively small temperature change (48.9 °C versus 51.1 °C in Case A), which may be explained as follows: from Fig. 13, the temperature curves of Case A and Case B are almost identical before $L_f = 0.3$ at which the PCM around the tube and fins is melted, as indicated in Fig. 5; at this stage, the tube and fins have a primary effect on heat transfer; after that, the temperature in Case B is lower than in Case A because the effective thermal conductivity in Case B is high, so heat can be easily transferred from the central to the side, without requiring a high temperature to drive heat transfer. As a result, the temperature change is lower. Compared to Case E, the temperature change is decreased by 1.0 °C in Case B and 1.2 °C in Case F, while that is increased by 1.2 °C in Case A.

In discharging, the final average temperature in Case A is 34.4 °C, and the temperature change is 39.7 °C, while they are 34.5 °C and 37.2 °C in Case F, respectively. Case B has a similar final temperature (34.7 °C) to Case A and a smaller temperature change (37.2 °C). These results indicate that the fin-stone hybrid has satisfactory temperature stability. As Table 7 shows, all these three cases have a higher temperature change than Case E, which is 7.4 °C, 4.9 °C, and 4.9 °C higher, respectively. That is because the final average temperature in Case E is higher, leading to a small temperature change.

For practical applications, the yearly energy supplied by a heat storage unit is calculated by the following formula:

$$Q_{year} = \frac{D}{t_{full}} Q_{res} \tag{18}$$

where D is the yearly operating time of a heat storage unit; t_{full} is the time of full charging and discharging; Q_{res} is the energy released in discharging because it is the energy supplied by the heat storage unit and utilised in practice. It is assumed that the heat storage unit is always in operation, and t_{full} is the sum of charging and discharging times predicted in this simulation. The initial conditions of charging may vary in different cycles; however, the eight cases use the same initial conditions and are compared with each other, so the effect of the difference in initial conditions should be negligible.

From Fig. 14, Case E supplies the least energy due to the poor heat transfer performance (23.8 MJ/year). After adding fins, i.e., Case A, the yearly supplied energy increases by 114%, reaching 50.9 MJ/year. Stones have a similar effect with different outcomes: the yearly energy in Cases F, G, and H is 65.4 MJ/year, 43.9 MJ/year, and 62.3 MJ/year, which is 175%, 84%, and 162% higher than in Case E, respectively. Case F with 20 mm-sized stones supplies more energy than Case A (28%), while Case G with 30 mm-sized stones supplies less energy (−14%), probably because small stones have small volumes, meaning that there can be more stones in the annulus; moreover, they have large surface areas and are in contact with the tube, which all contribute to heat transfer. The fin-stone hybrid structure further improves the yearly supplied energy. Compared to Case A, the yearly supplied energy increases by 121%, 67%, and 76% in Case B, Case C, and Case D, respectively. Although the energy capacity in Case B is less than in Case A, there is more charging and discharging over a year, leading to more supplied energy.

Since the density of stones is higher than that of paraffin, the mass of different cases based on the same 40 mm length is compared and listed in Table 8. Cases with the fin-stone hybrid structure have higher weight, where Case B, Case C, and Case D are 94%, 75%, and 67% heavier than Case A, respectively. However, they are not necessarily heavier than cases with stones because Case D has fewer stones than Case H. Hence, the fin-stone hybrid structure is suitable for on-site thermal energy storage where thermal energy is collected and utilised at the same place, without transport, such as on-site waste heat recovery [54] and residential building application [60].

4. Conclusions

A novel fin-stone hybrid structure integrating fins (popular thermal enhancers) and natural stones (widely used sensible heat storage media), which has advantages of low cost, environmental friendliness, and easy accessibility, is developed in this study to enhance the heat transfer of phase change materials for on-site thermal energy storage applications. 3D models of eight cases with various configurations, including the fin-stone hybrid structure, fins, stones, and no heat transfer enhancement, are constructed, and melting front, temperature response and the time-varying liquid fraction and thermal energy in charging and discharging are discussed. The following conclusions are drawn:

(1) Compared to fins, the fin-stone hybrid structure leads to a faster melting front propagation, especially the one with 20 mm-sized stones that makes a difference to the temperature distribution from the early stage, owing to stones' small volume, large surface area, and contact with the tube and fins. Hybrid structures with 20 mm-, 30 mm-, and 40 mm-sized stones save the charging time by 67%, 54%, and 56%, and the discharging time by 73%, 60%, and 46%, respectively.
(2) The fin-stone hybrid structure with 20 mm-sized stones has 44% shorter charging time and 30% shorter discharging time than stones. The results of 20 mm- and 30 mm-sized cases indicate that the hybrid structure has better heat transfer enhancement in charging than in discharging, which is attributed to the conjoint enhancement of heat conduction and natural convection in charging.
(3) The hybrid structure shows satisfactory temperature stability, where the temperature change is 48.9 °C in charging and 37.2 °C in discharging, each lower than the fins, which is desirable to stabilise the heat transfer fluid outlet temperature. The yearly supplied energy of the hybrid structure with 20 mm-sized stones is the most, 121% and 72% more than that of fins and stones, respectively.

CRediT authorship contribution statement

Shuai Zhang: Conceptualization, Investigation, Methodology, Writing – original draft. **Yuying Yan:** Conceptualization, Funding acquisition, Methodology, Supervision, Writing – review & editing. **Ziming Cheng:** Conceptualization, Methodology, Validation, Writing – review & editing. **Fuqiang Wang:** Conceptualization, Investigation, Methodology, Writing – review & editing.

Declaration of competing interest

The authors declare that they have no known competing financial interests or personal relationships that could have appeared to influence the work reported in this paper.

Data availability

Data will be made available on request.

Acknowledgements

The work has been supported by H2020-MSCA-RISE-778104–ThermaSMART and Royal Society (IEC\NSFC\211210).

Appendix A

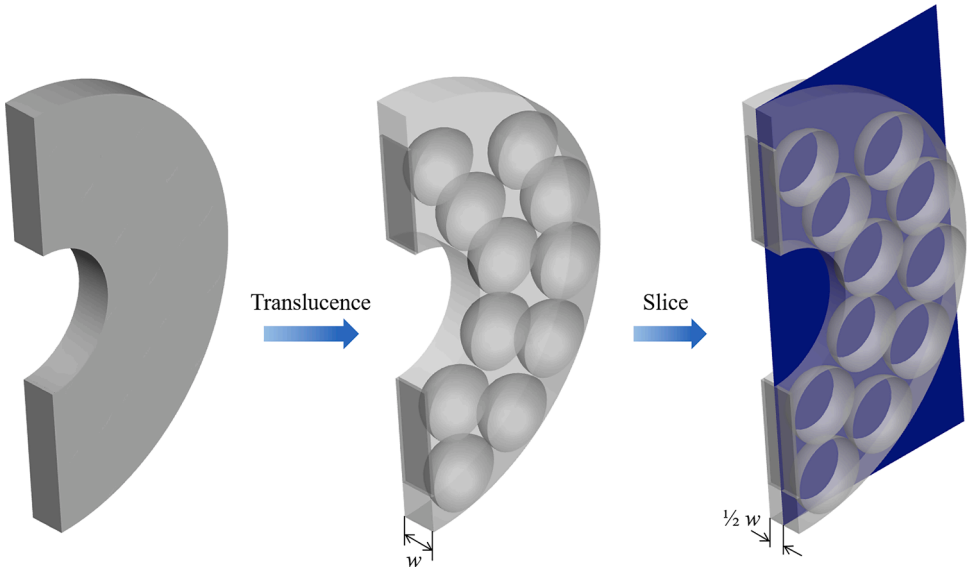

Fig. A1. Schematic of the plane position for the melting front and temperature field visualization.

Appendix B

The latent heat energy of the PCM is calculated by:

$$LE_{PCM} = m_{PCM} \cdot L \tag{B-1}$$

The sensible heat energy of the PCM is:

$$SE_{PCM} = m_{PCM} \cdot c_{p,\ PCM} \cdot (\overline{T}_{PCM} - T_{ini,\ PCM}) \tag{B-2}$$

where $\overline{T}_{PCM}$ is the average PCM temperature at the end of charging or discharging; $T_{ini,\ PCM}$ is the initial PCM temperature at the start of charging or discharging; m_{PCM} is the mass of the PCM:

$$m_{PCM} = V_{PCM} \cdot \rho_{PCM} = \frac{\pi\left(D_{shell}{}^2 - D_{tube}{}^2\right)}{4} \cdot l_{cal} \cdot \varepsilon \cdot \rho_{PCM} \tag{B-3}$$

where l_{cal} is the calculation length, taken as 40 mm in the current study. The sensible heat energy of fins and stones is calculated by:

$$SE_{fin} = m_{fin} \cdot c_{p,fin} \cdot (\overline{T}_{fin} - T_{ini,\ fin}) \tag{B-4}$$

$$SE_{stone} = m_{stone} \cdot c_{p,stone} \cdot (\overline{T}_{stone} - T_{ini,\ stone}) \tag{B-5}$$

where $\overline{T}_{fin}$ and $\overline{T}_{stone}$ is the average temperature of fins and stones at the end of charging or discharging, respectively. The mass of fins and stones are calculated by:

$$m_{fin} = V_{fin} \cdot \rho_{fin} = 2\omega h \cdot l_{cal} \cdot \rho_{fin} \tag{B-6}$$

$$m_{stone} = V_{stone} \cdot \rho_{stone} = \frac{\pi d^3}{6} N \cdot \frac{l_{cal}}{d} \cdot \rho_{stone} \tag{B-7}$$

The energy storage rate R_{sto} is:

$$R_{sto} = \frac{Q_{sto}}{t_{sto}} = \frac{LE_{PCM} + SE_{PCM} + SE_{fin} + SE_{stone}}{t_{sto}} \tag{B-8}$$

where t_{sto} is the charging time. $\overline{T}_{PCM}$ and $T_{ini,\ PCM}$ in SE_{PCM} are the ones in charging. The case is the same for SE_{fin} and SE_{stone}.

The energy release rate R_{res} is:

$$R_{res} = \frac{Q_{res}}{t_{res}} = \frac{LE_{PCM} + SE_{PCM} + SE_{fin} + SE_{stone}}{t_{res}} \tag{B-9}$$

where t_{res} is the discharging time. $\overline{T}_{PCM}$ and $T_{ini,\ PCM}$ in SE_{PCM} are the ones in discharging. The case is the same for SE_{fin} and SE_{stone}.

References

[1] S. Zhang, D. Feng, L. Shi, L. Wang, Y. Jin, L. Tian, Z. Li, G. Wang, L. Zhao, Y. Yan, A review of phase change heat transfer in shape-stabilized phase change materials (ss-PCMs) based on porous supports for thermal energy storage, Renew. Sustain. Energy Rev. 135 (2021) 110127.

[2] G. Alva, L. Liu, X. Huang, G. Fang, Thermal energy storage materials and systems for solar energy applications, Renew. Sustain. Energy Rev. 68 (2017) 693–706.

[3] Z. Cheng, H. Han, F. Wang, Y. Yan, X. Shi, H. Liang, X. Zhang, Y. Shuai, Efficient radiative cooling coating with biomimetic human skin wrinkle structure, Nano Energy 89 (2021) 106377.

[4] S. Bell, T. Steinberg, G. Will, Corrosion mechanisms in molten salt thermal energy storage for concentrating solar power, Renew. Sustain. Energy Rev. 114 (2019) 109328.

[5] M. Aramesh, B. Shabani, On the integration of phase change materials with evacuated tube solar thermal collectors, Renew. Sustain. Energy Rev. 132 (2020) 110135.

[6] S. Zhang, Y. Yao, Y. Jin, Z. Shang, Y. Yan, Heat transfer characteristics of ceramic foam/molten salt composite phase change material (CPCM) for medium-temperature thermal energy storage, Int. J. Heat Mass Transf. 196 (2022) 123262.

[7] S. Rostami, M. Afrand, A. Shahsavar, M. Sheikholeslami, R. Kalbasi, S. Aghakhani, M.S. Shadloo, H.F. Oztop, A review of melting and freezing processes of PCM/nano-PCM and their application in energy storage, Energy (2020) 118698.

[8] M.J. Li, M.J. Li, X.D. Xue, D. Li, Optimization and design criterion of the shell-and-tube thermal energy storage with cascaded PCMs under the constraint of outlet threshold temperature, Renew. Energy 181 (2022) 1371–1385.

[9] Y. Grosu, Y. Zhao, A. Giacomello, S. Meloni, J.L. Dauvergne, A. Nikulin, E. Palomo, Y. Ding, A. Faik, Hierarchical macro-nanoporous metals for leakage-free high-thermal conductivity shape-stabilized phase change materials, Appl. Energy 269 (2020) 115088.

[10] B. Palmer, A. Arshad, Y. Yang, C. Wen, Energy storage performance improvement of phase change materials-based triplex-tube heat exchanger (TTHX) using liquid–solid interface-informed fin configurations, Appl. Energy 333 (2023) 120576.

[11] A. Gautam, R.P. Saini, A review on sensible heat based packed bed solar thermal energy storage system for low temperature applications, Sol. Energy 207 (2020) 937–956.

[12] M.S. Audi, Experimental study of a solar space heating model using Jordanian rocks for storage, Energy Convers. Manag. 33 (1992) 833–842.

[13] R. Tiskatine, R. Oaddi, R. Ait El Cadi, A. Bazgaou, L. Bouirden, A. Aharoune, A. Ihlal, Suitability and characteristics of rocks for sensible heat storage in CSP plants, Sol. Energy Mater. Sol. Cells 169 (2017) 245–257.

[14] R. Lugolole, A. Mawire, D. Okello, K.A. Lentswe, K. Nyeinga, A.B. Shobo, Experimental analyses of sensible heat thermal energy storage systems during discharging, Sustain. Energy Technol. Assess. 35 (2019) 117–130.

[15] S. Soprani, F. Marongiu, L. Christensen, O. Alm, K.D. Petersen, T. Ulrich, K. Engelbrecht, Design and testing of a horizontal rock bed for high temperature thermal energy storage, Appl. Energy 251 (2019) 113345.

[16] P.L. Singh, S.D. Deshpandey, P.C. Jena, Thermal performance of packed bed heat storage system for solar air heaters, Energy Sustain. Dev. 29 (2015) 112–117.

[17] S. Zhang, Z. Li, H. Wang, L. Tian, Y. Jin, M. Alston, Y. Yan, Component-dependent thermal properties of molten salt eutectics for solar thermal energy storage: experiments, molecular simulation and applications, Appl. Therm. Eng. 209 (2022) 118333.

[18] S. Zhang, Y. Yan, Energy, exergy and economic analysis of ceramic foam-enhanced molten salt as phase change material for medium- and high-temperature thermal energy storage, Energy 262 (2023) 125462.

[19] Y. Yao, H. Wu, Macroscale modeling of solid–liquid phase change in metal foam/paraffin composite: effects of paraffin density treatment, thermal dispersion, and interstitial heat transfer, J. Therm. Sci. Eng. Appl. 13 (2021) 041024.

[20] Y. Yao, H. Wu, Z. Liu, Z. Gao, Pore-scale visualization and measurement of paraffin melting in high porosity open-cell copper foam, Int. J. Therm. Sci. 123 (2018) 73–85.
[21] A. Diani, M. Campanale, Transient melting of paraffin waxes embedded in aluminum foams: experimental results and modeling, Int. J. Therm. Sci. 144 (2019) 119–128.
[22] A. Atal, Y. Wang, M. Harsha, S. Sengupta, Effect of porosity of conducting matrix on a phase change energy storage device, Int. J. Heat Mass Transf. 93 (2016) 9–16.
[23] S. Zhang, Z. Li, Y. Yao, L. Tian, Y. Yan, Heat transfer characteristics and compatibility of molten salt/ceramic porous composite phase change material, Nano Energy 100 (2022) 107476.
[24] S. Zhang, Y. Yan, Evaluation of discharging performance of molten salt/ceramic foam composite phase change material in a shell-and-tube latent heat thermal energy storage unit, Renew. Energy 198 (2022) 1210–1223.
[25] H. Shabgard, T.L. Bergman, N. Sharifi, A. Faghri, High temperature latent heat thermal energy storage using heat pipes, Int. J. Heat Mass Transf. 53 (2010) 2979–2988.
[26] E.B.S. Mettawee, G.M.R. Assassa, Thermal conductivity enhancement in a latent heat storage system, Sol. Energy 81 (2007) 839–845.
[27] M. Al-Jethelah, S. Ebadi, K. Venkateshwar, S.H. Tasnim, S. Mahmud, A. Dutta, Charging nanoparticle enhanced bio-based PCM in open cell metallic foams: an experimental investigation, Appl. Therm. Eng. 148 (2019) 1029–1042.
[28] W.G. Alshaer, S.A. Nada, M.A. Rady, E.P. Del Barrio, A. Sommier, Thermal management of electronic devices using carbon foam and PCM/nano-composite, Int. J. Therm. Sci. 89 (2015) 79–86.
[29] M. Parsazadeh, X. Duan, Numerical study on the effects of fins and nanoparticles in a shell and tube phase change thermal energy storage unit, Appl. Energy 216 (2018) 142–156.
[30] A.M. Abdulateef, S. Mat, J. Abdulateef, K. Sopian, A.A. Al-Abidi, Geometric and design parameters of fins employed for enhancing thermal energy storage systems: a review, Renew. Sustain. Energy Rev. 82 (2018) 1620–1635.
[31] X. Yang, X. Wang, Z. Liu, X. Luo, J. Yan, Effect of fin number on the melting phase change in a horizontal finned shell-and-tube thermal energy storage unit, Sol. Energy Mater. Sol. Cells 236 (2022) 111527.
[32] M.M. Joybari, F. Haghighat, S. Seddegh, A.A. Al-Abidi, Heat transfer enhancement of phase change materials by fins under simultaneous charging and discharging, Energy Convers. Manag. 152 (2017) 136–156.
[33] P. Wang, H. Yao, Z. Lan, Z. Peng, Y. Huang, Y. Ding, Numerical investigation of PCM melting process in sleeve tube with internal fins, Energy Convers. Manag. 110 (2016) 428–435.
[34] Y.B. Tao, Y.L. He, Effects of natural convection on latent heat storage performance of salt in a horizontal concentric tube, Appl. Energy 143 (2015) 38–46.
[35] C. Liu, D. Groulx, Experimental study of the phase change heat transfer inside a horizontal cylindrical latent heat energy storage system, Int. J. Therm. Sci. 82 (2014) 100–110.
[36] C. Zhang, J. Li, Y. Chen, Improving the energy discharging performance of a latent heat storage (LHS) unit using fractal-tree-shaped fins, Appl. Energy 259 (2020) 114102.
[37] M. Sheikholeslami, S. Lohrasbi, D.D. Ganji, Numerical analysis of discharging process acceleration in LHTESS by immersing innovative fin configuration using finite element method, Appl. Therm. Eng. 107 (2016) 154–166.
[38] Z. Liu, Z. Liu, J. Guo, F. Wang, X. Yang, J. Yan, Innovative ladder-shaped fin design on a latent heat storage device for waste heat recovery, Appl. Energy 321 (2022) 119300.
[39] J. Zhang, Z. Cao, S. Huang, X. Huang, K. Liang, Y. Yang, H. Zhang, M. Tian, M. Akrami, C. Wen, Improving the melting performance of phase change materials using novel fins and nanoparticles in tubular energy storage systems, Appl. Energy 322 (2022) 119416.
[40] A. Sharma, C. Ding, S. Chul Kim, R. Chauhan, Investigation and optimization of solidification performance of concentration tube type latent heat storage unit with herringbone wavy fin designs, Appl. Therm. Eng. 222 (2023) 119924.
[41] M. Sheikholeslami, R.U. Haq, A. Shafee, Z. Li, Heat transfer behavior of nanoparticle enhanced PCM solidification through an enclosure with V shaped fins, Int. J. Heat Mass Transf. 130 (2019) 1322–1342.
[42] A. Sciacovelli, F. Gagliardi, V. Verda, Maximization of performance of a PCM latent heat storage system with innovative fins, Appl. Energy 137 (2015) 707–715.
[43] L. Wu, X. Zhang, X. Liu, Numerical analysis and improvement of the thermal performance in a latent heat thermal energy storage device with spiderweb-like fins, J. Energy Storage 32 (2020) 101768.
[44] S. Zhang, Y. Yan, Y. Jin, Y. Gao, Comprehensive thermal energy storage analysis of ceramic foam-enhanced molten salt in a shell-and-tube unit, Sol. Energy 255 (2023) 381–395.
[45] Z. Duan, Z. Zhang, J. Wang, X. Cao, J. Zhang, Thermal performance of structured packed bed with encapsulated phase change materials, Int. J. Heat Mass Transf. 158 (2020) 120066.
[46] W.J. Luo, P. Vishwakarma, B. Panigrahi, Hydrodynamic influence on thermal management of flexible heatsink devices embedded with out-of-plane intricate microchannel design, Int. Commun. Heat Mass Transf. 144 (2023) 106792.
[47] P. Zhang, Z.N. Meng, H. Zhu, Y.L. Wang, S.P. Peng, Melting heat transfer characteristics of a composite phase change material fabricated by paraffin and metal foam, Appl. Energy 185 (2017) 1971–1983.
[48] J. Yang, L. Yang, C. Xu, X. Du, Numerical analysis on thermal behavior of solid–liquid phase change within copper foam with varying porosity, Int. J. Heat Mass Transf. 84 (2015) 1008–1018.
[49] R. Ge, Q. Li, C. Li, Q. Liu, Evaluation of different melting performance enhancement structures in a shell-and-tube latent heat thermal energy storage system, Renew. Energy 187 (2022) 829–843.
[50] L. Pu, S. Zhang, L. Xu, Z. Ma, X. Wang, Numerical study on the performance of shell-and-tube thermal energy storage using multiple PCMs and gradient copper foam, Renew. Energy 174 (2021) 573–589.
[51] J.M. Mahdi, E.C. Nsofor, Solidification enhancement in a triplex-tube latent heat energy storage system using nanoparticles-metal foam combination, Energy 126 (2017) 501–512.
[52] S. Zhang, Y. Yan, Y. Jin, Y. Gao, Comprehensive thermal energy storage analysis of ceramic foam-enhanced molten salt in a shell-and-tube unit, Sol. Energy (2023).
[53] Ansys help: the Boussinesq model, https://ansyshelp.ansys.com/account/secured?returnurl=/Views/Secured/corp/v211/en/flu_ug/flu_ug_sec_hxfer_buoy.html?q=Boussinesq, 2023.
[54] Y. Huang, Z. Deng, Y. Chen, C. Zhang, Performance investigation of a biomimetic latent heat thermal energy storage device for waste heat recovery in data centers, Appl. Energy 335 (2023) 120745.
[55] S. Zhang, Z. Li, Y. Yan, M. Alston, L. Tian, Comparative study on heat transfer enhancement of metal foam and fins in a shell-and-tube latent heat thermal energy storage unit, Energy Storage Sav. 2 (2023) 487–494.
[56] M. Caliano, N. Bianco, G. Graditi, L. Mongibello, Analysis of a phase change material-based unit and of an aluminum foam/phase change material composite-based unit for cold thermal energy storage by numerical simulation, Appl. Energy 256 (2019) 113921.
[57] S. Zhang, Y. Yan, Evaluation and optimisation of hybrid sensible-latent heat thermal energy storage unit with natural stones to enhance heat transfer, Renew. Energy 215 (2023) 118921.
[58] S. Zhang, Y. Yan, Thermal performance of latent heat energy storage system with/without enhancement under solar fluctuation for organic Rankine power cycle, Energy Convers. Manag. 270 (2022) 116276.
[59] A.A. Al-Abidi, S. Mat, K. Sopian, M.Y. Sulaiman, A.T. Mohammad, Numerical study of PCM solidification in a triplex tube heat exchanger with internal and external fins, Int. J. Heat Mass Transf. 61 (2013) 684–695.
[60] L.T. Terziotti, M.L. Sweet, J.T. McLeskey, Modeling seasonal solar thermal energy storage in a large urban residential building using TRNSYS 16, Energy Build. 45 (2012) 28–31.